

Neuronal Attention Circuit (NAC) for Representation Learning

Waleed Razzaq¹ Izis Kankaraway¹ Yun-Bo Zhao^{1,2}

Abstract

Attention improves representation learning over RNNs, but its discrete nature limits continuous-time (CT) modeling. We introduce Neuronal Attention Circuit (NAC), a novel, biologically plausible CT-Attention mechanism that reformulates attention logits computation as the solution to a linear first-order ODE with nonlinear interlinked gates derived from repurposing *C. elegans* Neuronal Circuit Policies (NCPs) wiring mechanism. NAC replaces dense projections with sparse sensory gates for key-query projections and a sparse backbone network with two heads for computing *content-target* and *learnable time-constant* gates, enabling efficient adaptive dynamics. NAC supports three attention logit computation modes: (i) explicit Euler integration, (ii) exact closed-form solution, and (iii) steady-state approximation. To improve memory intensity, we implemented a sparse Top- K pairwise concatenation scheme that selectively curates key-query interactions. We provide rigorous theoretical guarantees, including state stability, bounded approximation errors, and universal approximation. Empirically, we implemented NAC in diverse domains, including irregular time-series classification, lane-keeping for autonomous vehicles, and industrial prognostics. We observed that NAC matches or outperforms competing baselines in accuracy and occupies an intermediate position in runtime and memory efficiency compared with several CT baselines.

1. Introduction

Learning representations of sequential data in temporal or spatio-temporal domains is essential for capturing patterns and enabling accurate forecasting. Discrete-time Recurrent neural networks (DT-RNNs) such as RNN (Rumelhart et al., 1985; Jordan, 1997), Long-short term memory

¹Department of Automation, University of Science & Technology of China, Hefei, China ²Institute of Artificial Intelligence, Hefei Comprehensive National Science Center. Correspondence to: Yun-Bo Zhao <ybzhao@ustc.edu.cn>, Waleed Razzaq <waleedrazzaq@mail.ustc.edu.cn>.

(LSTM) (Hochreiter & Schmidhuber, 1997), and Gated Recurrent Unit (GRU) (Cho et al., 2014) model sequential dependencies by iteratively updating hidden states to represent or predict future elements in a sequence. While effective for regularly sampled sequences, DT-RNNs face challenges with irregularly sampled data because they assume uniform time intervals. In addition, vanishing gradients can make it difficult to capture long-term dependencies (Hochreiter, 1998).

Continuous-time RNNs (CT-RNNs) (Rubanova et al., 2019) model hidden states as ordinary differential equations (ODEs), allowing them to process inputs that arrive at arbitrary or irregular time intervals. Mixed-memory RNNs (mmRNNs) (Lechner & Hasani, 2022) build on this idea by separating memory compartments from time-continuous states, helping maintain stable error propagation while capturing continuous-time dynamics. Liquid neural networks (LNNs) (Hasani et al., 2021; 2022) take a biologically inspired approach by assigning variable time-constants to hidden states, improving adaptability and robustness, though vanishing gradients can still pose challenges during training. The attention mechanisms (Vaswani et al., 2017) mitigate this limitation by treating all time steps equally and allowing models to focus on the most relevant observations. It computes the similarity between queries (q) and keys (k), scaling by the key dimension to keep gradients stable. Multi-Head Attention (MHA) (Vaswani et al., 2017) extends this by allowing the model to attend to different representation subspaces in parallel. Variants like Sparse Attention (Tay et al., 2020; Roy et al., 2021), BigBird (Zaheer et al., 2020), and Longformer (Beltagy et al., 2020) modify the attention pattern to reduce computational cost, particularly for long sequences, by attending only to selected positions rather than all pairs. Even with these improvements, attention-based methods still rely on discrete scaled dot-product operations, limiting their ability to model continuous trajectories often captured by CT counterparts.

Recent work has explored bridging this gap through Neural-ODE (Chen et al., 2018) formulation. mTAN (Shukla & Marlin, 2021) learns CT embeddings and uses time-based attention to interpolate irregular observations into a fixed-length representation for downstream encoder-decoder modeling. ODEFormer (d’Ascoli et al., 2023) trains a sequence-to-sequence transformer on synthetic trajectories to directly infer symbolic ODE systems from noisy, irregular data, though it struggles with chaotic systems and generalization

beyond observed conditions. Continuous-time Attention (CTA) (Chien & Chen, 2021) embeds a continuous-time attention mechanism within a Neural ODE, allowing attention weights and hidden states to evolve jointly over time. Still, it remains computationally intensive and sensitive to the accuracy of the ODE solver. ContiFormer (Chen et al., 2023) builds a CT-transformer by pairing ODE-defined latent trajectories with a time-aware attention mechanism to model dynamic relationships in data.

Despite these innovations, a persistent and underexplored gap remains in developing a biologically plausible attention mechanism that seamlessly integrates CT dynamics with the abstraction of the brain’s connectome to handle irregular sequences without prohibitive computational costs. Building on this, we propose a novel attention mechanism called the *Neuronal Attention Circuit* (NAC), in which attention logits are computed as the solution to a first-order ODE modulated by nonlinear, interlinked gates derived from repurposing Neuronal Circuit Policies (NCPs) from the nervous system of *C. elegans* nematode (refer to Appendix A.2 for more information). Unlike standard attention, which projects key-query pairs through a dense layer, NAC employs a sensory gate to transform input features and a backbone to model nonlinear interactions, with multiple heads producing outputs structured for attention logits computation. Based on the solutions to ODE, we define three computation modes: (i) Exact, using the closed-form ODE solution; (ii) Euler, approximating the solution via *explicit Euler* integration; and (iii) Steady, using only the steady-state solution, analogous to standard attention scores. To reduce computational complexity, we implemented a sparse Top- K pairwise concatenation algorithm that selectively curates key-query inputs. We evaluate NAC across multiple domains, including irregularly sampled time series, autonomous vehicle lane-keeping, and Industry 4.0, comparing it to state-of-the-art baselines. NAC consistently matches or outperforms these models, while runtime and peak memory benchmarks place it between CT-RNNs in terms of speed and CT-Attentions in terms of memory requirements.

2. Neuronal Attention Circuit (NAC)

We propose a simple alternative formulation of the attention logits a (refer to Appendix A.1 for more information), interpreting them as the solution to a first-order linear ODE modulated by nonlinear, interlinked gates:

$$\frac{da_t}{dt} = - \underbrace{f_{\omega_\tau}([\mathbf{q}; \mathbf{k}], \theta_{\omega_\tau})}_{\omega_\tau(\mathbf{u})} a_t + \underbrace{f_\phi([\mathbf{q}; \mathbf{k}], \theta_\phi)}_{\phi(\mathbf{u})}, \quad (1)$$

where $\mathbf{u} = [\mathbf{q}; \mathbf{k}]$ denotes the sparse Top- K concatenated query-key input. ω_τ represents a learnable time-constant gate head, ϕ denotes a nonlinear content-target head. Both gates are parameterized by a backbone network derived

from repurposing NCPs. We refer to this formulation as the Neuronal Attention Circuit (NAC). It enables the logits a_t to evolve dynamically with input-dependent, variable time constants, mirroring the adaptive temporal dynamics found in *C. elegans* nervous systems while improving computational efficiency and expressiveness. Moreover, it introduces continuous depth into the attention mechanism, bridging discrete-layer computation with dynamic temporal evolution.

Motivation behind this formulation: The proposed formulation is loosely motivated by the input-dependent time-constant mechanism of Liquid Neural Networks (LNNs), a class of CT-RNNs inspired by biological nervous systems and synaptic transmission. In this framework, the dynamics of non-spiking neurons are described by a linear ODE with nonlinear, interlinked gates: $\frac{d\mathbf{x}_t}{dt} = \frac{\mathbf{x}_t}{\tau} + \mathbf{S}_t$, where \mathbf{x}_t denotes the hidden state and $\mathbf{S}_t \in \mathbb{R}^M$ represents a nonlinear contribution defined as $f(\mathbf{x}_t, \mathbf{u}, t, \theta)(A - \mathbf{x}_t)$. Here, A and θ are learnable parameters. Plugging \mathbf{S}_t yields $\frac{d\mathbf{x}_t}{dt} = -[-\frac{1}{\tau} - f(\mathbf{x}_t, \mathbf{u}, t, \theta)] \mathbf{x}_t + f(\mathbf{x}_t, \mathbf{u}, t, \theta)A$. LNNs are known for their strong expressivity, stability, and performance in irregularly sampled time-series modeling (Hasani et al., 2021; 2022).

NAC’s forward-pass update using ODE solver: The state of NAC at time t can be computed using a numerical ODE solver that simulates the dynamics from an initial state a_0 to a_t . The solver discretizes the continuous interval $[0, T]$ into steps $[t_0, t_1, t_2, \dots, t_n]$, with each step updating the state from t_i to t_{i+1} . For our purposes, we use the *explicit Euler* solver, which is simple, efficient, and easy to implement. Although methods such as Runge-Kutta may offer higher accuracy, their computational overhead makes them less suitable for large-scale neural simulations that require numerous updates, especially since the logits are normalized, and exact precision is not necessary. Let the step size be Δt , with discrete times $t_n = n\Delta t$ and logit states $a_n = a(t_n)$. Using the *explicit Euler* method, the update is

$$a_{n+1} = a_n + \Delta t (-\omega_\tau a_n + \phi). \quad (2)$$

Closed-form (Exact) Computation of NAC: We now devise the analytical solution for Eqn. 1. Let both ω_τ and ϕ be fixed in pseudo-time interval (frozen-coefficient approximation (John, 1952)) with initial condition a_0 , then closed-form solution is:

$$a_t = \underbrace{a^*}_{\text{steady-state}} + \underbrace{(a_0 - a^*) e^{-\omega_\tau t}}_{\text{transient}} \quad (3)$$

Here, $a^* = \phi/\omega_\tau$ is the steady-state solution. The full derivation is provided in Appendix B.1.

2.1. Stability Analysis of NAC

We now investigate the stability bounds of *NAC* under both the ODE-based and the Closed-Form formulations.

2.1.1. STATE STABILITY

We analyze state stability in both single-connection and multi-connection settings. This analysis establishes the boundedness of the attention logit state trajectory, ensuring that, under positive decay rates, the dynamics remain well-behaved without divergence or overshoot.

Theorem 1 (State Stability). *Let $a_t^{(i)}$ denote the state of the i -th attention logit governed by $\dot{a}_t^{(i)}/dt = -\omega_\tau a_t^{(i)} + \phi$. Assume that ϕ and ω_τ decompose across M incoming connections as $\phi = \sum_{j=1}^M f_\phi([\mathbf{q}_i; \mathbf{k}_j])$, and $\omega_\tau = \sum_{j=1}^M f_{\omega_\tau}([\mathbf{q}_i; \mathbf{k}_j])$, with $f_{\omega_\tau} > 0$. Define the per-connection equilibrium $A_{i,j} = f_\phi([\mathbf{q}_i; \mathbf{k}_j])/f_{\omega_\tau}([\mathbf{q}_i; \mathbf{k}_j])$, and let $A_i^{\min} = \min_j A_{i,j}$ and $A_i^{\max} = \max_j A_{i,j}$. Then for any finite horizon $t \in [0, T]$, the state trajectory satisfies*

$$\min(0, A_i^{\min}) \leq a_t^{(i)} \leq \max(0, A_i^{\max}), \quad (4)$$

provided the initial condition $a_i(0)$ lies within this range. In the special case of a single connection ($M = 1$), the bounds collapse to

$$\min(0, A_i) \leq a_t^{(i)} \leq \max(0, A_i), \quad (5)$$

where $A_i = f_\phi/\omega_\tau$ is exactly the steady-state solution from Eqn. 3. The proof is provided in the Appendix B.2.

2.1.2. CLOSED-FORM ERROR & EXPONENTIAL BOUNDS

We now examine the asymptotic stability, error characterization, and exponential boundedness of the closed-form formulation. We begin by quantifying the deviation of the trajectory from its steady-state solution. Define the instantaneous error

$$\varepsilon_t = a_t - a^*, \quad (6)$$

which measures the distance of the system state to equilibrium at time t . From Eqn. 3, the error admits the exact representation

$$\varepsilon_t = (a_0 - a^*)e^{-\omega_\tau t} \quad (7)$$

In particular, the pointwise absolute error is given by

$$|\varepsilon_t| = |a_0 - a^*| e^{-\omega_\tau t} \quad (8)$$

This reveals that convergence is not merely asymptotic but follows an exact exponential law, controlled by the rate parameter ω_τ . This yields the following finite-time guarantee.

Corollary 1 (Exponential decay bound). *If $\omega_\tau > 0$, then for all $t \geq 0$,*

$$|a_t - a^*| \leq |a_0 - a^*| e^{-\omega_\tau t}. \quad (9)$$

Remark: If $\omega_\tau > 0$ then $\lim_{t \rightarrow \infty} e^{-\omega_\tau t} = 0$, therefore $a_t \rightarrow a^*$. The convergence is exponential with rate ω_τ . If $\omega_\tau < 0$ then $e^{-\omega_\tau t} = e^{|\omega_\tau|t}$ diverges so a_t grows exponentially away from a^* in magnitude (unless initial offset $a_0 - a^* = 0$, a measure-zero case). If $\omega_\tau = 0$ the ODE is $\dot{a} = \phi$ and the solution is linear in t (unless $\phi = 0$). For bounded dynamics that converge to an interpretable steady-state, it is required that $\omega_\tau > 0$.

Corollary 2 (Uniform initialization). *If the initialization is only known to belong to a bounded set, i.e., $|a_0 - a^*| \leq M$ for some $M > 0$, then the error admits the uniform bound*

$$|a_t - a^*| \leq M e^{-\omega_\tau t}. \quad (10)$$

Remark: This bound highlights that exponential convergence holds uniformly across all admissible initial conditions, with the constant M capturing the worst-case deviation.

Corollary 3 (Sample complexity to δ -accuracy). *A natural operational question is the time required to achieve a target tolerance $\delta > 0$. Solving*

$$|a_0 - a^*| e^{-\omega_\tau t} \leq \delta, \quad (11)$$

We obtain the threshold

$$t \geq \frac{1}{\omega_\tau} \ln \frac{|a_0 - a^*|}{\delta}. \quad (12)$$

Remark: The convergence rate is inversely proportional to ω_τ , and the required time scales only logarithmically in the accuracy level $1/\delta$. Intuitively, larger ω_τ accelerates contraction towards equilibrium, yielding faster attainment of any prescribed tolerance.

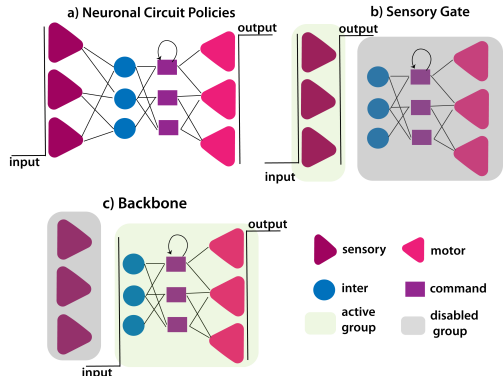


Figure 1. Illustration of (a) NCPs with pre-determined wiring; (b) Sensory Gate, where sensory neurons are active, and the remaining neurons are disabled for the q , k , and v projections; (c) Backbone, showing inter-motor projections with sensory neurons disabled in extended heads for computing ϕ and ω_τ .

Algorithm 1 Repurposed NCPCell

Require: Wiring \mathcal{W} with $(A_{\text{in}}, A_{\text{rec}})$, groups (N_s, N_i, N_c, N_m) , activation α , input group G_{input} , output group G_{output} , disabled groups \mathcal{D}

Ensure: Output $y_t \in \mathbb{R}^{B \times d_{\text{out}}}$, state $\mathbf{x}_t \in \mathbb{R}^{B \times d_h}$

Binary mask: $M_{\text{rec}} \leftarrow |A_{\text{rec}}|$, $M_{\text{in}} \leftarrow |A_{\text{in}}|$

Initialize parameters: $W_{\text{in}}, W_{\text{rec}}, b, w_{\text{in}}, b_{\text{in}}, w_{\text{out}}, b_{\text{out}}$

Input neurons: $I_{\text{in}} \leftarrow G_{\text{input}}$

Output neurons: $I_{\text{out}} \leftarrow G_{\text{output}}$

Define activation mask: $\text{mask}_{\text{act},i} = 0$ if $i \in \mathcal{D}$ else 1

Input Projections: $\tilde{u}_t \leftarrow u_t \odot w_{\text{in}} + b_{\text{in}}$

Recurrent computation: $r_t \leftarrow \mathbf{x}_{t-1}(W_{\text{rec}} \odot M_{\text{rec}})$

Sparse computation: $s_t \leftarrow \tilde{u}_t(W_{\text{in}} \odot M_{\text{in}})$

Neuron update: $\mathbf{x}_t \leftarrow \alpha(r_t + s_t + b) \odot \text{mask}_{\text{act}}$

Output mapping: $y_t \leftarrow (\mathbf{x}_t[I_{\text{out}}] \odot w_{\text{out}}) + b_{\text{out}}$

return (y_t, \mathbf{x}_t)

Algorithm 2 Sparse Top- K Pairwise Concatenation

Require: Keys $K \in \mathbb{R}^{B \times H \times T_k \times D}$, Top- K value K

Ensure: concatenated tensor $U \in \mathbb{R}^{B \times H \times T_q \times K_{\text{eff}} \times 2D}$

Scores: $S \leftarrow Q \cdot K^{\top}$

Effective Top- K : $K_{\text{eff}} \leftarrow \min(K, T_k)$

Indices: $I_{\text{topk}} \leftarrow \text{top_k}(S, K_{\text{eff}})$

Gather: $K_{\text{selected}} \leftarrow \text{gather}(K, I_{\text{topk}}) \in \mathbb{R}^{B \times H \times T_q \times K_{\text{eff}} \times D}$

Tiled: $Q_{\text{tiled}} \leftarrow \text{tile}(Q, K_{\text{eff}}) \in \mathbb{R}^{B \times H \times T_q \times K_{\text{eff}} \times D}$

Concatenate: $U_{\text{topk}} \leftarrow [Q_{\text{tiled}}; K_{\text{selected}}] \in \mathbb{R}^{B \times H \times T_q \times K_{\text{eff}} \times 2D}$

return U_{topk}

2.2. Designing the Neural Network

We now outline the design of a neural network layer guided by the preceding analysis. The process involves five steps: (i) repurposing NCPs; (ii) input curation; (iii) construction of the time vector (t); (iv) computing attention logits and weights; and (v) generating the attention output. Figure 2 provides a graphical overview of NAC.

Repurposing NCPs: We repurpose the NCPs framework by converting its fixed, biologically derived wiring (see Figure 1(a)) into a flexible recurrent architecture that allows configurable input–output mappings. Instead of enforcing a static connectome, our approach exposes adjacency matrices as modifiable structures defining sparse input and recurrent connections. This enables selective information routing across neuron groups while retaining the original circuit topology. Decoupling wiring specifications from model instantiation allows dynamic connectivity adjustments to accommodate different input modalities without full retraining. Algorithm 1 summarizes the steps for repurposing the NCPs wiring mechanism. Key features include group-wise masking for neuron isolation, adaptive remapping of inputs and outputs for task-specific adaptation, and tunable sparsity s to balance expressiveness and efficiency.

In our implementation, the sensory neuron gate ($\mathcal{NN}_{\text{sensory}}$) projects the q , k , and v representations (see Figure 1(b)). This enables sensory neurons to maintain structured, context-aware representations rather than collapsing inputs into fully

connected layers. As a result, the network preserves locality and modularity, which improves information routing.

$$\begin{aligned} \mathcal{NN}_{\text{sensory}} &= \text{NCPCell}(G_{\text{input}} = [N_s], G_{\text{output}} = [N_s], \\ &\quad \mathcal{D} = [N_i, N_c, N_m], s) \end{aligned} \quad (13)$$

The inter-to-motor pathways form a backbone network ($\mathcal{NN}_{\text{backbone}}$) with branches that compute ϕ and ω_{τ} (see Figure 1(c)). Instead of learning ϕ and ω_{τ} independently, this backbone allows the model to learn shared representations, enabling multiple benefits: (i) separate head layers enable the system to capture temporal and structural dependencies independently; (ii) accelerates convergence during training.

$$\begin{aligned} \mathcal{NN}_{\text{backbone}} &= \text{NCPCell}(G_{\text{input}} = [N_i], G_{\text{output}} = [N_m], \\ &\quad \mathcal{D} = [N_s], s) \end{aligned} \quad (14)$$

The output heads are defined as:

$$\phi = \sigma(\mathcal{NN}_{\text{backbone}}(\mathbf{u})) \quad (15)$$

$$\omega_{\tau} = \text{softplus}(\mathcal{NN}_{\text{backbone}}(\mathbf{u})) + \varepsilon, \quad \varepsilon > 0 \quad (16)$$

Here, ϕ serves as a *content–target gate* head, where the sigmoid function $\sigma(\cdot)$ determines the target signal strength. In contrast, ω_{τ} is a strictly positive *time–constant gate* head that controls the rate of convergence and the steady-state amplitude. Conceptually, this parallels recurrent gating: ϕ regulates *what* content to emphasize, while ω_{τ} governs *how quickly* and *to what extent* it is expressed.

Input Curation: We experimented with different strategies for constructing query–key inputs. Initially, we implemented full pairwise concatenation, where queries $Q \in \mathbb{R}^{B \times H \times T_q \times D}$ are combined with all keys $K \in \mathbb{R}^{B \times H \times T_k \times D}$ to form a joint tensor $U \in \mathbb{R}^{B \times H \times T_q \times T_k \times 2D}$. While this preserved complete feature information and enabled expressive, learnable similarity functions, it was memory-intensive, making it impractical for longer sequences. To mitigate this, we applied a sparse Top- K optimization: for each query, we compute pairwise scores $S = Q \cdot K^{\top} \in \mathbb{R}^{B \times H \times T_q \times T_k}$, select the Top- $K_{\text{eff}} = \min(K, T_k)$ keys, and construct concatenated pairs $U_{\text{topk}} \in \mathbb{R}^{B \times H \times T_q \times K_{\text{eff}} \times 2D}$. This approach preserves the most relevant interactions while substantially reducing memory requirements in the concatenation and subsequent backbone processing stages, allowing the method to scale linearly with the sequence length in those components. However, the initial computation of S remains quadratic (see Appendix C.3). Algorithm 2 outlines the steps required for input curation.

Time Vector: NAC builds on continuous-depth models as (Hasani et al., 2022) that adapt their temporal dynamics to the task. It constructs an internal, normalized pseudo-time vector t_{pseudo} using a sigmoidal transformation, $t_{\text{pseudo}} = \sigma(t_a \cdot t + t_b)$, where t_a and t_b are learnable affine

parameters and σ is the sigmoid function. For time-varying datasets (e.g., irregularly sampled series), each time point t is derived from the sample’s timestamp, while for tasks without meaningful timing, t is set to 1. The resulting t_{pseudo} lies in $[0, 1]$ and provides a smooth, bounded representation of time for modulating the network’s dynamics.

Attention logits and weights: Starting from Eqn. 3, consider the trajectory of a query–key pair with initial condition $a_0 = 0$:

$$a_t = \frac{\phi}{\omega_\tau} (1 - e^{-\omega_\tau t}), \quad (17)$$

For finite t , the exponential factor $(1 - e^{-\omega_\tau t})$ regulates the buildup of attention, giving ω_τ a temporal gating role. Normalizing across all keys via *softmax* yields attention weights $\alpha_t = \text{softmax}(a_t)$, defining a valid probability distribution where ϕ amplifies or suppresses content alignments, and ω_τ shapes both the speed and saturation of these preferences. As $t \rightarrow \infty$, the trajectory converges to the steady state

$$a_t^* = \frac{\phi}{\omega_\tau} \approx \frac{q^\top k}{\sqrt{d_k}}, \quad (18)$$

which is analogous to scaled-dot attention under specific parameterization when the backbone $\mathcal{NN}_{\text{backbone}}$ is configured as a linear projection such that $\phi(u) = q^\top k$ and $\omega_\tau(u) = \sqrt{d_k}$ (e.g., by setting NCP weights to emulate bilinear forms and disabling nonlinearities). In general, the nonlinear backbone allows for more expressive similarities, with the approximation holding when trained to mimic dot products.

Attention output: Finally, the attention output is computed by integrating the attention weights with the value matrix:

$$\text{NAC}(q, k, v) = \int_T \alpha_t v_t dt \quad (19)$$

In practice, the integration is approximated using a Riemann-style approach, where the weighted elements are computed by multiplying each v_t with its corresponding α_t . These are then summed and multiplied by a fixed pseudo-time step δ_t , chosen as a scalar (typically between 0.5–1.0) hyperparameter during layer initialization. This yields a continuous analogue of standard weighted sums, giving finer resolution of the attention trajectory without altering the underlying values. Sensitivity to attention output w.r.t δ_t is visualized in Appendix D.2.

2.2.1. EXTENSION TO MULTI-HEAD

To scale this mechanism to multi-head attention, we project the input sequence into H independent subspaces (heads) of dimension d_{model}/H , yielding query, key, and value tensors $(q^{(h)}, k^{(h)}, v^{(h)})$ for $h \in \{1, \dots, H\}$. For each head, pairwise logits are computed according to Eqns. 2, 3 or 18,

followed by the *softmax* normalization to calculate attention weights. The resulting attention weights $\alpha_t^{(h)}$ are then used to integrate with the value vector $v^{(h)}$, producing head-specific attention outputs. Finally, these outputs are concatenated and linearly projected back into the model dimension. This formulation ensures that each head learns distinct dynamic compatibilities governed by its own parameterization of ϕ and ω_τ , while the aggregation across heads preserves the expressive capacity of the standard multi-head attention mechanism.

2.3. NAC as Universal Approximator

We now establish the universal approximation capability of NAC by extending the classical Universal Approximation Theorem (UAT) (Nishijima, 2021) to the proposed mechanism. For brevity, we consider a network with a single NAC layer processing fixed-dimensional inputs, though the argument generalizes to sequences.

Theorem 2 (Universal Approximation by NAC). *Let $K \subset \mathbb{R}^n$ be a compact set and $f : K \rightarrow \mathbb{R}^m$ be a continuous function. For any $\epsilon > 0$, there exists a neural network consisting of a single NAC layer, with sufficiently large model dimension d_{model} , number of heads H , sparsity s , and nonlinear activations, such that the network’s output $g : \mathbb{R}^n \rightarrow \mathbb{R}^m$ satisfies*

$$\sup_{x \in K} \|f(x) - g(x)\| < \epsilon. \quad (20)$$

The proof is provided in Appendix B.3.

3. Evaluation

We evaluate the proposed architecture against a range of baselines, including (DT & CT) RNN, (DT & CT) attention, and multiple NAC ablation configurations. Experiments are conducted across diverse domains, including irregular time-series modeling, lane keeping of autonomous vehicles, and Industry 4.0 prognostics. All results are obtained using 5-fold cross-validation, where models are trained using BPTT (see Appendix C.2) on each fold and evaluated across all folds. We report the mean (μ) and standard deviation (σ) to capture variability and quantify uncertainty in the predictions. Table 1 provides results for all experiments, and the details of the baselines, ablation, environment utilized, the data curation and preprocessing, and neural network architectures for all experiments are provided in the Appendix D.3.

3.1. Irregular Time-series

We evaluate the proposed architecture on two irregular time-series datasets: (i) Event-based MNIST; and (ii) Person Activity Recognition (PAR).

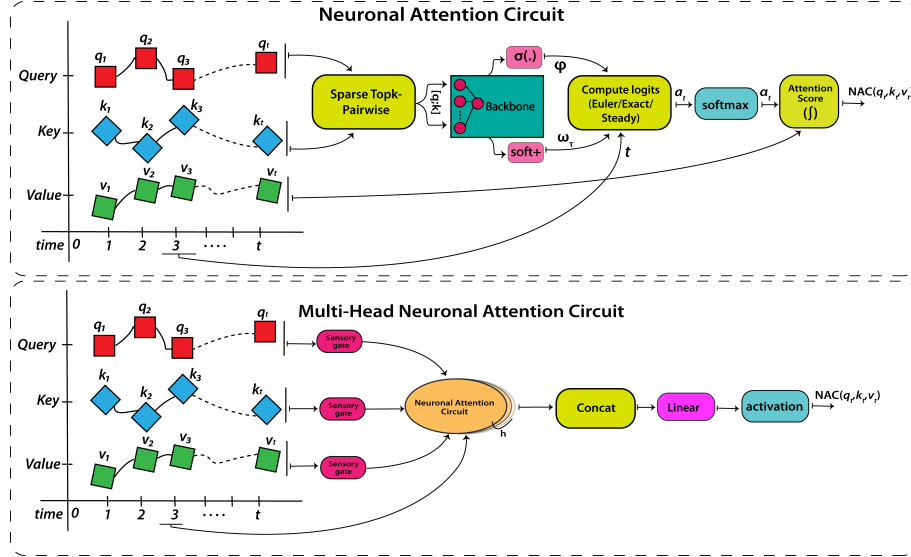


Figure 2. Illustration of the architecture of (a) Neuronal Attention Circuit mechanism ; (b) Multi-Head Extension

Event-based MNIST: Event-based MNIST is the transformation of the widely recognized MNIST dataset with irregular sampling added originally proposed in (Lechner & Hasani, 2022). The transformation was done in two steps: (i) flattening each 28×28 image into a time series of length 784, and (ii) encoding the binary time series into an event-based format by collapsing consecutive identical values (e.g., 1,1,1,1 \rightarrow (1, t=4)). This representation requires models to handle temporal dependencies effectively. NAC-PW achieved first place with an accuracy of 96.64%, followed by NAC-Exact/05s/8k at 96.12%. GRU-ODE and ContiFormer ranked third with 96.04%.

Person Activity Recognition (PAR): We employed the Localized Person Activity dataset from UC Irvine (Vidulin et al., 2010). The dataset contains data from five participants, each equipped with inertial measurement sensors sampled every 211 ms. The goal of this experiment is to predict a person’s activity from a set of predefined actions, making it a classification task. All models performed well on this task, with NAC-PW achieving 89.15% accuracy and taking first place. NAC-Exact/05s/8k and GRU-ODE ranked second with 89.01% accuracy, while NAC-02s ranked third with 88.84% mean accuracy.

3.2. Lane-Keeping of Autonomous Vehicles

Lane keeping in autonomous vehicles (AVs) is a fundamental problem in robotics and AI. Early works (Tiang et al., 2018; Park et al., 2021) primarily emphasized accuracy, often relying on large models. More recent research (Lechner et al., 2020; Razzaq & Hongwei, 2023) has shifted toward designing compact architectures suitable for resource-constrained devices. The goal of this experiment is to create a long causal structure between the road’s horizon and the

corresponding steering commands. To evaluate, we used two widely adopted simulation environments: (i) OpenAI CarRacing (Brockman et al., 2016); and (ii) the Udacity Self-Driving Car Simulator (uda). In OpenAI CarRacing, the task is to classify steering actions from a predefined action set. In contrast, the Udacity Simulator requires predicting a continuous trajectory of steering values. We implemented the AI models proposed by (Razzaq & Hongwei, 2023), replacing the recurrent layer with NAC and its counterparts. All models achieved around 80% accuracy on average in the CarRacing benchmark. Notably, NAC-PW performed the best, reaching the highest accuracy of 80.72%, followed by NAC-Steady, ranked second with 80.62%. LSTM and GRU took third position, achieving 80.60% on average. In the Udacity benchmark, NAC-32k performed the best, achieving the lowest MSE of 0.0170. NAC-Exact followed with 0.0173, and ContiFormer ranked third with 0.0174. To visualize saliency maps for these experiments, refer to Appendix D.3.3. Experimental videos are available for the OpenAI CarRacing [click here] and for the Udacity Simulator [click here].

3.3. Industry 4.0

Industry 4.0 has transformed manufacturing, making prognostic health management (PHM) systems essential. A key PHM task is estimating the remaining useful life (RUL) of components, particularly rolling element bearings (REB), which account for 40–50% of machine failures (Ding et al., 2021; Zhuang et al., 2021). The objective is to learn degradation features from one operating condition of a dataset and generalize to unseen conditions within the same dataset. Furthermore, the model should provide accurate RUL estimation on entirely different datasets, while maintaining a

Table 1. Model Performance Across All Categories and Datasets

Model	Irregular Time-Series		Lane-Keeping of AVs		Industry 4.0		
	E-MNIST (\uparrow)	PAR (\uparrow)	CarRacing (\uparrow)	Udacity (\downarrow)	PRONOSTIA (\downarrow)	XJTU-SY (\downarrow)	HUST (\downarrow)
RNN	95.59 \pm 0.37	88.77 \pm 0.58	78.90 \pm 3.35	0.0210 \pm 0.0014	42.05 \pm 7.49	31.07 \pm 6.63	42.22 \pm 8.16
LSTM	95.88 \pm 0.23	88.36 \pm 0.79	80.60 \pm 0.12	0.0181 \pm 0.0014	41.87 \pm 2.88	31.99 \pm 8.32	44.09 \pm 2.14
GRU	95.85 \pm 0.22	88.68 \pm 1.35	80.60 \pm 0.22	0.0206 \pm 0.0014	44.22 \pm 4.60	26.65 \pm 4.49	41.86 \pm 7.96
CT-RNN	95.18 \pm 0.20	88.71 \pm 0.87	80.21 \pm 0.27	0.0206 \pm 0.0013	44.32 \pm 8.69	26.01 \pm 8.74	39.99 \pm 6.33
GRU-ODE	96.04\pm0.13	89.01\pm1.55	80.29 \pm 0.72	0.0188 \pm 0.0016	45.11 \pm 3.19	31.20 \pm 8.69	43.91 \pm 7.10
PhasedLSTM	95.79 \pm 0.14	88.93 \pm 1.08	80.35 \pm 0.38	0.0186 \pm 0.0015	44.15 \pm 4.80	35.49 \pm 5.54	38.66 \pm 5.55
mmRNN	95.74 \pm 0.27	88.48 \pm 0.46	80.13 \pm 0.54	0.0205 \pm 0.0027	48.50 \pm 4.60	27.84 \pm 4.05	40.11 \pm 9.56
LTC	95.25 \pm 0.00	88.12 \pm 0.68	76.37 \pm 3.01	0.0245 \pm 0.0024	48.14 \pm 5.01	36.83 \pm 8.57	61.82 \pm 15.64
CfC	94.16 \pm 0.49	88.60 \pm 0.34	80.59 \pm 0.33	0.0198 \pm 0.0022	47.78 \pm 3.54	35.51 \pm 3.94	54.09 \pm 10.13
Attention	95.68 \pm 0.23	88.29 \pm 0.98	80.40 \pm 0.26	0.0193 \pm 0.0009	41.89 \pm 6.98	26.29 \pm 4.06	40.28 \pm 4.23
MHA	95.94 \pm 0.15	88.36 \pm 1.06	79.99 \pm 0.49	0.0185 \pm 0.0017	45.36 \pm 5.16	37.31 \pm 12.20	41.40 \pm 7.72
mTAN	95.97 \pm 0.25	88.08 \pm 0.94	80.86 \pm 0.22	0.0178 \pm 0.0005	44.41 \pm 7.15	41.34 \pm 3.72	66.29 \pm 4.25
CTA	95.86 \pm 0.14	88.10 \pm 1.10	80.54 \pm 0.40	0.0197 \pm 0.0016	39.16 \pm 3.54	25.86\pm1.47	38.41 \pm 4.51
ODEFormer	95.62 \pm 0.20	88.25 \pm 0.66	80.54 \pm 0.40	0.0190 \pm 0.0012	42.42 \pm 6.98	35.63 \pm 9.24	40.60 \pm 6.83
ContiFormer	96.04\pm0.23	81.28 \pm 0.85	80.47 \pm 0.50	0.0174\pm0.01	27.82\pm7.09	34.71 \pm 4.98	43.81 \pm 10.18
NAC-2k	95.73 \pm 0.07	88.84% \pm 0.81	80.59 \pm 0.46	0.0208 \pm 0.0015	43.78 \pm 2.71	37.43 \pm 9.28	40.51 \pm 6.61
NAC-32k	95.15 \pm 0.11	88.80 \pm 0.76	80.38 \pm 0.16	0.0170\pm0.0007	49.53 \pm 4.89	32.45 \pm 10.84	39.17 \pm 12.23
NAC-PW	96.64\pm0.12	89.15\pm1.01	80.72\pm0.41	0.0177 \pm 0.0008	37.50\pm2.56	28.01 \pm 4.93	30.14\pm6.87
NAC-FC	95.31 \pm 0.07	88.45 \pm 0.91	80.49 \pm 0.46	0.0192 \pm 0.0012	40.36 \pm 6.09	24.89\pm5.30	35.35\pm6.64
NAC-02s	95.31 \pm 0.07	88.84 \pm 1.33	80.47 \pm 0.27	0.0188 \pm 0.0013	39.43 \pm 5.94	35.59 \pm 3.86	38.90 \pm 6.43
NAC-09s	95.86 \pm 0.11	88.61% \pm 1.25	80.43% \pm 0.17	0.0188 \pm 0.0013	47.29 \pm 5.52	40.40 \pm 8.85	44.39 \pm 6.82
NAC-Exact/05s/8k	96.12\pm0.11	89.01\pm1.01	80.59 \pm 1.82	0.0173\pm0.0006	37.75\pm4.72	19.87\pm1.75	27.82\pm7.09
NAC-Euler	95.67 \pm 0.26	88.52 \pm 0.68	80.61\pm0.28	0.0181 \pm 0.0017	42.08 \pm 6.14	28.46 \pm 8.18	39.32 \pm 9.15
NAC-Steady	95.75 \pm 0.28	88.36 \pm 1.05	80.62\pm0.26	0.0181 \pm 0.0012	40.95 \pm 5.77	26.76 \pm 7.36	37.12 \pm 12.43

Note: (\uparrow) higher is better; (\downarrow) lower is better.

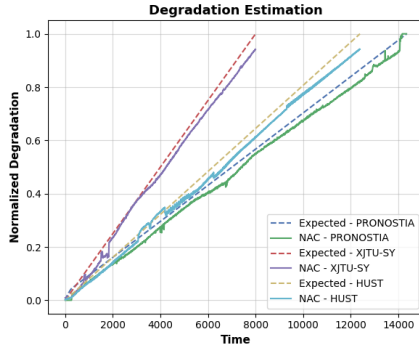


Figure 3. Degradation Estimation Results.

compact architecture suitable for resource-constrained devices, thereby supporting localized safety.

We utilized three benchmark datasets: (i) PRONOSTIA (Nectoux et al., 2012), (ii) XJTU-SY (Wang et al., 2018), and (iii) HUST (Thuan & Hong, 2023). Training is performed on PRONOSTIA, while XJTU-SY and HUST are used to assess cross-validation. We used the Score metric (Nectoux et al., 2012) to assess the performance. We evaluate generalization using *Bearing 1* from the first operating condition of each dataset. Figure 3 visualizes the expected degradation alongside the outputs of NAC. On the PRONOSTIA dataset, ContiFormer performed the best with

the lowest score of 27.82. NAC-Exact/05s/8k and NAC-PW achieved nearly identical scores, obtaining 37.75 and 37.50 on average, respectively. On the XJTU-SY dataset, NAC-Exact/05s/8k has the lowest score of 19.87. NAC-FC ranked second with a score of 24.89, followed by NAC-PW in third place with an average score of 28.01. A similar trend was observed on the HUST dataset, where NAC-Exact/05s/8k achieved first place with a score of 27.82, NAC-PW ranked second with 30.14, and NAC-FC ranked third with 35.35. These results demonstrated the strong cross-validation capability of NAC.

3.4. Run Time and Memory Experiments

We evaluate computational requirements on fixed-length sequences of 1024 steps, 64-dimensional features, 4 heads, and a Batch size of 1. Each model is run for ten forward passes on Google Colab T4-GPU, and we report the mean runtime with standard deviation, throughput, and peak memory usage. NAC occupies an intermediate position in runtime relative to several CT-RNN models, including GRU-ODE, CfC, and LTC. In terms of memory consumption, NAC uses significantly less memory than mTAN, with NAC-2k being the least memory-consuming among the CT-Attention models. Reducing NAC sparsity from 90% to 20% has minimal effect on memory, decreasing usage slightly

Table 2. Run-Time and Memory Benchmark Results

Model	Run-Time (s)	Throughput (seq/s)	Peak Memory (MB)
RNN	1.8392 \pm 0.1933	0.544	0.29
CT-RNN	7.1097 \pm 0.3048	0.141	0.67
LSTM	2.6241 \pm 0.2906	0.381	0.42
PhasedLSTM	4.9812 \pm 0.272	0.201	0.80
GRU	3.216 \pm 0.2566	0.311	0.54
GRU-ODE	12.2498 \pm 0.0525	0.082	0.64
mmRNN	7.5852 \pm 0.2785	0.132	0.96
LTC	14.643 \pm 0.2445	0.068	0.99
CfC	6.0988 \pm 0.2135	0.164	0.76
Attention	0.0016 \pm 0.0001	625.00	16.86
MHA	0.0041 \pm 0.0001	243.90	69.05
mTAN	0.0272 \pm 0.0054	36.76	790.16
ODEFormer	0.0317 \pm 0.0016	31.55	67.71
CTA	8.5275 \pm 0.2355	0.117	1.43
ContiFormer	0.066 \pm 0.0075	15.15	67.71
NAC-2k	7.3071 \pm 0.1547	0.137	44.75
NAC-32k	7.2313 \pm 0.219	0.138	549.86
NAC-PW	8.5649 \pm 0.0203	0.117	5042.09
NAC-FC	0.0195 \pm 0.0002	51.28	29.92
NAC-02s	7.252 \pm 0.2018	0.138	151.54
NAC-09s	7.222 \pm 0.176	0.139	150.85
NAC-Exact/05s/8k	7.4101 \pm 0.1586	0.135	151.50
NAC-Euler	7.3367 \pm 0.1719	0.136	152.22
NAC-Steady	7.2942 \pm 0.1451	0.137	150.86

from 151.54 MB to 150.85 MB. In contrast, decreasing the Top- K selection from PW to $k = 2$ drastically reduces memory consumption from 5042 MB to 44.75 MB, demonstrating the flexibility of NAC.

Interpreting the Results: From the experiments, we observe that increasing the sparsity of the NAC layer improves the robustness of the system and leads to higher overall accuracy. Similarly, increasing the Top- K interactions enhances accuracy too; however, the benefits diminish as memory consumption grows. Using Exact mode, Top- K =8 with 50% sparsity achieves the best balance between accuracy and efficiency. Steady mode is the fastest, while Euler mode handles adaptive temporal dynamics.

4. Discussions

This research is part of ongoing work on biologically plausible attention mechanisms and represents a pioneering step, with limitations to be addressed in future work.

Architectural improvement: Currently, NAC uses pre-determined wiring (AutoNCP) requiring three inputs: number of units (sensory + interneuron + motor), output motor neurons, and sparsity, with typically 60% of units assigned to sensory neurons. To integrate with the attention mechanism while preserving wiring, sensory units for $\mathcal{N}\mathcal{N}_{\text{sensory}}$ are set as $\text{units}_{\text{sensory}} = \lceil \frac{d_{\text{model}} - 0.5}{0.6} \rceil$ and backbone units as $\text{units}_{\text{backbone}} = d_{\text{model}} + \lfloor \frac{d_{\text{model}}}{0.6} \rfloor$, where $\lceil \cdot \rceil$ and $\lfloor \cdot \rfloor$ denote the ceiling and floor functions, respectively. This results in a larger overall architectural size and increased runtime.

Future work will support user-defined NCPs configurations or randomized wiring to enable more efficient architectures.

Learnable sparse Top- K selection: Sparse Top- K attention can miss important context, is sensitive to k , and may be harder to optimize. A further limitation is that it still computes the full QK^\top matrix, which can dominate the cost for very long sequences. Future work includes adaptive or learnable Top- K selection, improved key scoring, and hardware-aware optimization to strengthen accuracy and robustness.

5. Conclusion

In this paper, we introduce the Neuronal Attention Circuit (NAC), a biologically inspired attention mechanism that reformulates attention logits as the solution to a first-order ODE modulated by nonlinear, interlinked gates derived from repurposing *C.elegans* nematode NCPs. NAC bridges discrete attention with continuous-time dynamics, enabling adaptive temporal processing without the limitations inherent to traditional scaled dot-product attention. Based on the solution to ODE, we introduce three computational modes: (i) Euler, based on *explicit Euler* integration; (ii) Exact, providing closed-form solutions; and (iii) Steady, approximating equilibrium states. In addition, a sparse Top- K pairwise concatenation scheme is introduced to mitigate the memory intensity. Theoretically, we establish NAC’s log-state stability, exponential error bounds, and universal approximation, thereby providing rigorous guarantees of convergence and expressiveness. Empirical evaluations demonstrate that NAC achieves state-of-the-art performance across diverse tasks, including irregularly sampled time-series benchmarks, autonomous vehicle lane-keeping, and industrial prognostics. Moreover, NAC occupies an intermediate position between CT-RNNs and CT-Attention, offering robust temporal modeling while requiring less runtime than CT-RNNs and less memory than CT-Attention models.

Reproducibility Statement

The code for reproducibility is available at https://github.com/itxwaleedrazaq/neuronal_attention_circuit

Impact Statement

The work addresses the growing field of continuous-time attention and pioneers a biologically plausible mechanism. It encourages research into sparse, adaptive networks that resemble natural wiring. From a societal perspective, it supports more robust AI in resource-limited settings, but it also raises ethical concerns when applied to areas such as surveillance or autonomous systems.

References

Introduction to self-driving cars. URL <https://www.udacity.com/course/intro-to-self-driving-cars--nd113>.

Aguiar-Conraria, L. and Soares, M. J. The continuous wavelet transform: Moving beyond uni-and bivariate analysis. *Journal of economic surveys*, 28(2):344–375, 2014.

Beltagy, I., Peters, M. E., and Cohan, A. Longformer: The long-document transformer. *arXiv preprint arXiv:2004.05150*, 2020.

Bojarski, M., Del Testa, D., Dworakowski, D., Firner, B., Flepp, B., Goyal, P., Jackel, L. D., Monfort, M., Muller, U., Zhang, J., et al. End to end learning for self-driving cars. *arXiv preprint arXiv:1604.07316*, 2016.

Brockman, G., Cheung, V., Pettersson, L., Schneider, J., Schulman, J., Tang, J., and Zaremba, W. Openai gym. *arXiv preprint arXiv:1606.01540*, 2016.

Cao, Y., Li, S., Petzold, L., and Serban, R. Adjoint sensitivity analysis for differential-algebraic equations: The adjoint dae system and its numerical solution. *SIAM journal on scientific computing*, 24(3):1076–1089, 2003.

Chen, R. T., Rubanova, Y., Bettencourt, J., and Duvenaud, D. K. Neural ordinary differential equations. *Advances in neural information processing systems*, 31, 2018.

Chen, Y., Ren, K., Wang, Y., Fang, Y., Sun, W., and Li, D. Contiformer: Continuous-time transformer for irregular time series modeling. *Advances in Neural Information Processing Systems*, 36:47143–47175, 2023.

Chien, J.-T. and Chen, Y.-H. Continuous-time attention for sequential learning. In *Proceedings of the AAAI conference on artificial intelligence*, volume 35, pp. 7116–7124, 2021.

Cho, K., Van Merriënboer, B., Gulcehre, C., Bahdanau, D., Bougares, F., Schwenk, H., and Bengio, Y. Learning phrase representations using rnn encoder-decoder for statistical machine translation. *arXiv preprint arXiv:1406.1078*, 2014.

d’Ascoli, S., Becker, S., Mathis, A., Schwaller, P., and Kilbertus, N. Odeformer: Symbolic regression of dynamical systems with transformers. *arXiv preprint arXiv:2310.05573*, 2023.

De Brouwer, E., Simm, J., Arany, A., and Moreau, Y. Gru-ode-bayes: Continuous modeling of sporadically-observed time series. *Advances in neural information processing systems*, 32, 2019.

Deng, L. The mnist database of handwritten digit images for machine learning research [best of the web]. *IEEE signal processing magazine*, 29(6):141–142, 2012.

Ding, Y., Jia, M., Miao, Q., and Huang, P. Remaining useful life estimation using deep metric transfer learning for kernel regression. *Reliability Engineering & System Safety*, 212:107583, 2021.

Hasani, R., Lechner, M., Amini, A., Rus, D., and Grosu, R. Liquid time-constant networks. In *Proceedings of the AAAI Conference on Artificial Intelligence*, volume 35, pp. 7657–7666, 2021.

Hasani, R., Lechner, M., Amini, A., Liebenwein, L., Ray, A., Tschaikowski, M., Teschl, G., and Rus, D. Closed-form continuous-time neural networks. *Nature Machine Intelligence*, 4(11):992–1003, 2022.

Hochreiter, S. The vanishing gradient problem during learning recurrent neural nets and problem solutions. *International Journal of Uncertainty, Fuzziness and Knowledge-Based Systems*, 6(02):107–116, 1998.

Hochreiter, S. and Schmidhuber, J. Long short-term memory. *Neural computation*, 9(8):1735–1780, 1997.

Hong, H. S. and Thuan, N. Hust bearing: a practical dataset for ball bearing fault diagnosis. *Mendeley Data*, 3, 2023.

John, F. On integration of parabolic equations by difference methods: I. linear and quasi-linear equations for the infinite interval. *Communications on Pure and Applied Mathematics*, 5(2):155–211, 1952.

Jordan, M. I. Serial order: A parallel distributed processing approach. In *Advances in psychology*, volume 121, pp. 471–495. Elsevier, 1997.

Lechner, M. and Hasani, R. Mixed-memory rnns for learning long-term dependencies in irregularly sampled time series. 2022.

Lechner, M., Hasani, R. M., and Grosu, R. Neuronal circuit policies. *arXiv preprint arXiv:1803.08554*, 2018.

Lechner, M., Hasani, R., Amini, A., Henzinger, T. A., Rus, D., and Grosu, R. Neural circuit policies enabling auditable autonomy. *Nature Machine Intelligence*, 2(10):642–652, 2020.

LeCun, Y., Touresky, D., Hinton, G., and Sejnowski, T. A theoretical framework for back-propagation. In *Proceedings of the 1988 connectionist models summer school*, volume 1, pp. 21–28, 1988.

Lin, J. and Qu, L. Feature extraction based on morlet wavelet and its application for mechanical fault diagnosis. *Journal of sound and vibration*, 234(1):135–148, 2000.

Nectoux, P., Gouriveau, R., Medjaher, K., Ramasso, E., Chebel-Morello, B., Zerhouni, N., and Varnier, C. Pronostia: An experimental platform for bearings accelerated degradation tests. In *IEEE International Conference on Prognostics and Health Management, PHM'12.*, pp. 1–8. IEEE Catalog Number: CPF12PHM-CDR, 2012.

Neil, D., Pfeiffer, M., and Liu, S.-C. Phased lstm: Accelerating recurrent network training for long or event-based sequences. *Advances in neural information processing systems*, 29, 2016.

Nishijima, T. Universal approximation theorem for neural networks. *arXiv preprint arXiv:2102.10993*, 2021.

Park, M., Kim, H., and Park, S. A convolutional neural network-based end-to-end self-driving using lidar and camera fusion: Analysis perspectives in a real-world environment. *Electronics*, 10(21):2608, 2021.

Razzaq, W. and Hongwei, M. Neural circuit policies imposing visual perceptual autonomy. *Neural Processing Letters*, 55(7):9101–9116, 2023.

Razzaq, W. and Zhao, Y.-B. Carle: a hybrid deep-shallow learning framework for robust and explainable rul estimation of rolling element bearings. *Soft Computing*, 29(23): 6269–6292, 2025a.

Razzaq, W. and Zhao, Y.-B. Developing distance-aware uncertainty quantification methods in physics-guided neural networks for reliable bearing health prediction, 2025b. URL <https://arxiv.org/abs/2512.08499>.

Roy, A., Saffar, M., Vaswani, A., and Grangier, D. Efficient content-based sparse attention with routing transformers. *Transactions of the Association for Computational Linguistics*, 9:53–68, 2021.

Rubanova, Y., Chen, R. T., and Duvenaud, D. K. Latent ordinary differential equations for irregularly-sampled time series. *Advances in neural information processing systems*, 32, 2019.

Rumelhart, D. E., Hinton, G. E., and Williams, R. J. Learning internal representations by error propagation. Technical report, 1985.

Shibuya, N. Car behavioral cloning, 2017. URL <https://github.com/naokishibuya/car-behavioral-cloning>. Accessed: 2025-10-05.

Shukla, S. N. and Marlin, B. M. Multi-time attention networks for irregularly sampled time series. *arXiv preprint arXiv:2101.10318*, 2021.

Stinchcomb, M. Multilayered feedforward networks are universal approximators. *Neural Networks*, 2:356–359, 1989.

Tay, Y., Bahri, D., Yang, L., Metzler, D., and Juan, D.-C. Sparse sinkhorn attention. In *International conference on machine learning*, pp. 9438–9447. PMLR, 2020.

Thuan, N. D. and Hong, H. S. Hust bearing: a practical dataset for ball bearing fault diagnosis. *BMC research notes*, 16(1):138, 2023.

Tiang, Y., Gelernter, J. R., Wang, X., Chen, W., Gao, J., Zhang, Y., and Li, X. Lane marking detection via fast end-to-end deep convolutional neural network that is our patch proposal network (ppn). 2018.

Vaswani, A., Shazeer, N., Parmar, N., Uszkoreit, J., Jones, L., Gomez, A. N., Kaiser, Ł., and Polosukhin, I. Attention is all you need. *Advances in neural information processing systems*, 30, 2017.

Vidulin, V., Lustrek, M., Kaluza, B., Piltaver, R., and Krivec, J. Localization Data for Person Activity. UCI Machine Learning Repository, 2010. DOI: <https://doi.org/10.24432/C57G8X>.

Wang, B., Lei, Y., Li, N., et al. Xjtu-sy bearing datasets. *GitHub, GitHub Repository*, 2018.

Zaheer, M., Guruganesh, G., Dubey, K. A., Ainslie, J., Alberti, C., Ontanon, S., Pham, P., Ravula, A., Wang, Q., Yang, L., et al. Big bird: Transformers for longer sequences. *Advances in neural information processing systems*, 33:17283–17297, 2020.

Zhuang, J., Dvornek, N., Li, X., Tatikonda, S., Papademetris, X., and Duncan, J. Adaptive checkpoint adjoint method for gradient estimation in neural ode. In *International Conference on Machine Learning*, pp. 11639–11649. PMLR, 2020.

Zhuang, J., Jia, M., Ding, Y., and Ding, P. Temporal convolution-based transferable cross-domain adaptation approach for remaining useful life estimation under variable failure behaviors. *Reliability Engineering & System Safety*, 216:107946, 2021.

Appendix

A. Preliminaries

A.1. Attention Mechanism

Attention mechanisms have become a cornerstone in modern neural architectures, enabling models to dynamically focus on relevant parts of the input. The concept was first introduced in the context of neural machine translation, where it allowed the decoder to weight encoder outputs according to their importance for generating each target token. Formally, given a query vector $q \in \mathbb{R}^d$, key vectors $K = [k_1, k_2, \dots, k_n] \in \mathbb{R}^{n \times d}$, and value vectors $V = [v_1, v_2, \dots, v_n] \in \mathbb{R}^{n \times d}$, the attention mechanism can be expressed in two steps:

1. Compute the scaled dot attention logits:

$$a_i = \frac{q^T k_i}{\sqrt{d}} \quad (21)$$

2. Normalize the logits to get attention weights and compute the output:

$$\alpha_i = \text{softmax}(a_i) = \frac{e^{a_i}}{\sum_{j=1}^n e^{a_j}} \quad (22)$$

$$\text{Attention}(q, k, v) = \sum_{i=1}^n \alpha_i v_i \quad (23)$$

Here, a_i is the raw attention logit between the query and each key, and the scaling factor \sqrt{d} prevents large dot products from destabilizing the softmax (Vaswani et al., 2017).

A.2. Neuronal Circuit Policies (NCPs)

NCPs represent a biologically inspired framework for developing interpretable neural control agents by adapting the tap-withdrawal circuit found in the nematode *C. elegans* (Lechner et al., 2018). Unlike traditional spiking neural networks, the majority of neurons in this circuit exhibit electronic dynamics, characterized by the passive flow of electrical charges, resulting in graded potentials. NCPs are structured as a four-layer hierarchical architecture comprising sensory neurons (N_s), interneurons (N_i), command neurons (N_c), and motor neurons (N_m). The N_s perceive and respond to external stimulus inputs and are responsible for the initial signal transduction. Each N_s consists of subneurons S_p and S_n and a system variable x . The activation of S_p and S_n depends upon the sign of x : S_p becomes activated for $x > 0$, whereas S_n becomes activated for $x < 0$. The variable x is mapped to the membrane potential range of $[-70 \text{ mV}, -20 \text{ mV}]$, which is consistent with the biophysical behavior of nerve cells, which typically

exhibit a resting potential at -70 mV and an activation potential near -20 mV . Similarly, each N_m is composed of two subneurons, M_p and M_n , and is driven by a controllable variable y , which also maps to a biologically plausible range $[-70 \text{ mV}, -20 \text{ mV}]$. The connections in the NCP architecture are designed to reflect the biological sparsity and abstraction of neural circuits. Specifically, connections from N_s to N_i are feedforward, while those between N_c and N_m are highly recurrent (Lechner et al., 2018). Figure 1(a) illustrates the connectome of NCPs.

B. Proofs

In this section, we provide all the proofs.

B.1. Deriving Closed-form (Exact) Solution

Although ϕ and ω_τ are nonlinear functions of the input $\mathbf{u} = [\mathbf{q}; \mathbf{k}]$, we derive closed-form solution by treating them as locally constant over the pseudo-time integration interval for each query–key pair based on frozen-coefficient approximation (John, 1952). This is accurate whenever the interval is short or when input variations are slow compared with the relaxation rate ω_τ . Under approximation assumption, rewrite Eqn. 1 as

$$\frac{da_t}{dt} + \omega_\tau a_t = \phi. \quad (24)$$

This is now a linear first-order ODE. The integrating factor is

$$\mu = e^{\left(\int \omega_\tau dt\right)} = e^{\omega_\tau t}. \quad (25)$$

Multiply both sides by $\mu(t)$:

$$e^{\omega_\tau t} \frac{da_t}{dt} + \omega_\tau e^{\omega_\tau t} a_t = \phi e^{\omega_\tau t}. \quad (26)$$

Recognize the left-hand side as the derivative of $e^{\omega_\tau t} a_t$:

$$\frac{d}{dt}(e^{\omega_\tau t} a_t) = \phi e^{\omega_\tau t}. \quad (27)$$

Integrate from 0 to t :

$$e^{\omega_\tau t} a_t - e^0 a_0 = \phi \int_0^t e^{\omega_\tau s} ds. \quad (28)$$

Compute the integral (since $\omega_\tau \neq 0$):

$$\int_0^t e^{\omega_\tau s} ds = \frac{1}{\omega_\tau} (e^{\omega_\tau t} - 1). \quad (29)$$

Substitute back:

$$e^{\omega_\tau t} a_t - a_0 = \phi \cdot \frac{e^{\omega_\tau t} - 1}{\omega_\tau}. \quad (30)$$

Rearrange:

$$e^{\omega_\tau t} a_t = a_0 + \frac{\phi}{\omega_\tau} (e^{\omega_\tau t} - 1). \quad (31)$$

Divide both sides by $e^{\omega_\tau t}$:

$$a_t = a_0 e^{-\omega_\tau t} + \frac{\phi}{\omega_\tau} (1 - e^{-\omega_\tau t}). \quad (32)$$

Set $a^* := \frac{\phi}{\omega_\tau}$. Then $a_t = a^* + (a_0 - a^*) e^{-\omega_\tau t}$, proved.

B.2. Proof of Theorem 1

We divide the proof into two parts: (i) the single-connection case $M = 1$, and (ii) the general multi-connection case $M > 1$. The main technique is to evaluate the ODE at boundary values of the proposed invariant interval and show that the derivative points inward, ensuring that trajectories cannot escape.

CASE 1: SINGLE CONNECTION ($M = 1$).

The ODE reduces to

$$\frac{da}{dt} = -\omega_\tau a + \phi = -\omega_\tau(a - A), \quad A = \frac{\phi}{\omega_\tau}. \quad (33)$$

Here A is the unique equilibrium. We now check both bounds.

- *Upper bound*: Let $M = \max(0, A)$. At $a = M$,

$$\frac{da}{dt} \Big|_{a=M} = -\omega_\tau(M - A). \quad (34)$$

If $A \geq 0$, then $M = A$ and $\frac{da}{dt} = 0$. If $A < 0$, then $M = 0$, so $\frac{da}{dt} = -\omega_\tau(0 - A) = \omega_\tau A \leq 0$ since $A < 0$. In both cases, $\frac{da}{dt} \leq 0$. Thus trajectories cannot cross above M .

- *Lower bound*: Let $m = \min(0, A)$. At $a = m$,

$$\frac{da}{dt} \Big|_{a=m} = -\omega_\tau(m - A). \quad (35)$$

If $A \leq 0$, then $m = A$ and $\frac{da}{dt} = 0$. If $A > 0$, then $m = 0$, so $\frac{da}{dt} = -\omega_\tau(0 - A) = \omega_\tau A \geq 0$. In both cases, $\frac{da}{dt} \geq 0$. Thus trajectories cannot cross below m . Therefore, the interval $[m, M]$ is forward-invariant.

To see this explicitly under Euler discretization with step size $\Delta t > 0$,

$$a(t + \Delta t) = a_t + \Delta t \cdot \frac{da}{dt}. \quad (36)$$

At $a = M$, $\frac{da}{dt} \leq 0 \implies a(t + \Delta t) \leq M$. At $a = m$, $\frac{da}{dt} \geq 0 \implies a(t + \Delta t) \geq m$. By induction over steps, $a_t \in [m, M]$ for all $t \in [0, T]$.

CASE 2: MULTIPLE CONNECTIONS ($M > 1$).

The ODE is

$$\frac{da}{dt} = -\left(\sum_{j=1}^M f_j\right)a + \sum_{j=1}^M f_j A_j, \quad (37)$$

with per-connection equilibria $A_j = \phi_j/f_j$. The effective equilibrium is

$$A = \frac{\sum_{j=1}^M f_j A_j}{\sum_{j=1}^M f_j}. \quad (38)$$

Since the weights $\frac{f_j}{\sum f_j}$ are positive and sum to 1, A is a convex combination of $\{A_j\}$. Therefore,

$$A \in [A^{\min}, A^{\max}]. \quad (39)$$

- *Upper bound*: Let $M = \max(0, A^{\max})$. Then

$$\frac{da}{dt} \Big|_{a=M} = \sum_{j=1}^M f_j (A_j - M). \quad (40)$$

Since $A_j \leq A^{\max} \leq M$, each term $(A_j - M) \leq 0$, and thus $\sum f_j (A_j - M) \leq 0$. Hence $\frac{da}{dt} \leq 0$, proving trajectories cannot exceed M .

- *Lower bound*: Let $m = \min(0, A^{\min})$. Then

$$\frac{da}{dt} \Big|_{a=m} = \sum_{j=1}^M f_j (A_j - m). \quad (41)$$

Since $A_j \geq A^{\min} \geq m$, each $(A_j - m) \geq 0$, so $\sum f_j (A_j - m) \geq 0$. Hence $\frac{da}{dt} \geq 0$, proving trajectories cannot fall below m . Thus, the interval $[m, M]$ is forward-invariant.

Remark 1. This result guarantees that the continuous-time attention state converges within a well-defined interval dictated by the per-connection equilibria. In particular, for the single-connection case ($M = 1$), the state trajectory converges monotonically toward the closed-form equilibrium solution (Eqn. 18) without overshoot.

B.3. Proof for Theorem 2

The proof proceeds constructively by showing that the NAC layer can emulate a single-hidden-layer feedforward neural network with nonlinear activations, which is a universal approximator under the Universal Approximation Theorem (UAT). We assume self-attention on a single-token input $x \in \mathbb{R}^n$ (setting sequence length $T = 1$) and focus on the steady mode for simplicity. Without loss of generality, set $d_{\text{model}} = n + m$ or adjust as needed for dimensionality. Constructively, set NCP sparsity $s = 0$ for full connectivity, ensuring the backbone $\mathcal{NN}_{\text{backbone}}$ approximates any $\tilde{\phi} : \mathbb{R}^{2d} \rightarrow [0, 1]$ with error $< \delta$ via stacked layers. For

multi-head, scale H proportionally to target complexity, with output projection W_o aggregating as in classical UAT proofs (Stinchcomb, 1989).

Input Projections: The input x is projected via NCP-based sensory projections to obtain query $q = q_{\text{proj}}(x)$, key $k = k_{\text{proj}}(x)$, and value $v = v_{\text{proj}}(x)$, each in $\mathbb{R}^{d_{\text{model}}}$. For emulation, set $q_{\text{proj}} = k_{\text{proj}} = I_n$ (identity on \mathbb{R}^n) and adjust

Head Splitting and Sparse Top- k Pairwise Computation:

Split into H heads, yielding $q^{(h)}, k^{(h)} \in \mathbb{R}^d$ per head h , where $d = d_{\text{model}}/H$. For $T = 1$, compute sparse top- k pairs, but since $T = 1$, $K_{\text{eff}} = 1$, yielding concatenated pair $u^{(h)} = [q^{(h)}; k^{(h)}] \in \mathbb{R}^{2d}$. Since $q^{(h)} = k^{(h)}$, this is $[x^{(h)}; x^{(h)}]$, but the NCP processes it generally.

Computation of $\phi^{(h)}$ and $\omega_{\tau}^{(h)}$: The scalar $\phi^{(h)}$ is computed via the NCP-based inter-to-motor projection on the pair:

$$\phi^{(h)} = \sigma(\mathcal{NN}_{\text{backbone}}(u^{(h)})) \quad (42)$$

where $\sigma(z) = (1 + e^{-z})^{-1}$ is the sigmoid. This NCP, with sufficiently large units and low sparsity, approximates any continuous scalar function $\tilde{\phi} : \mathbb{R}^{2d} \rightarrow [0, 1]$ to arbitrary precision on compact sets (by the UAT for multi-layer networks (Stinchcomb, 1989)). Similarly, $\omega_{\tau}^{(h)}$ is computed via:

$$\omega_{\tau}^{(h)} = \text{softplus}(\mathcal{NN}_{\text{backbone}}(u^{(h)})) + \varepsilon, \quad \varepsilon > 0 \quad (43)$$

By setting weights to make $\omega_{\tau}^{(h)} \equiv 1$ (constant), the steady-mode logit simplifies to $a^{(h)} = \phi^{(h)}/\omega_{\tau}^{(h)} = \phi^{(h)}$. Thus, $a^{(h)} \approx \sigma(w^{(h)}x + b^{(h)})$ for chosen weights $w^{(h)}, b^{(h)}$, emulating a sigmoid hidden unit.

Attention Weights and output: For $T = 1$, the softmax over one “key” yields $\alpha^{(h)} = \exp(a^{(h)})/\exp(a^{(h)}) = 1$. The head output is $y^{(h)} = \int_T \alpha^{(h)} v^{(h)} dt$. Set v_{proj} such that $v^{(h)} = 1$ (scalar), yielding $y^{(h)} \approx \sigma(w^{(h)}x + b^{(h)})$. For vector-valued $v^{(h)}$, more complex combinations are possible, but scalars suffice here.

Output Projection: Concatenate head outputs: $Y = [y^{(1)}; y^{(2)}; \dots; y^{(H)}] \in \mathbb{R}^H$. Apply the final dense layer:

$$g(x) = (Y \cdot W_o) + b_o \in \mathbb{R}^m. \quad (44)$$

With $y^{(h)} \approx \sigma(w^{(h)}x + b^{(h)})$, this matches a single-hidden-layer network with H units. By the UAT, for large H , such networks approximate any continuous f on compact K to accuracy ϵ , by choosing appropriate $w^{(h)}, b^{(h)}, W_o, b_o$.

C. Training, Gradients and Complexity

C.1. Gradient Characterization

We analyze the sensitivity of the dynamics with respect to the underlying learnable parameters. Specifically, we compute closed-form derivatives of both the steady state and the full trajectory a_t with respect to the parameters ϕ and ω_{τ} . These expressions illuminate how gradients flow through

the system, and provide guidance for selecting parameterizations that avoid vanishing or exploding gradients.

C.1.1. TRAJECTORY SENSITIVITIES FOR CLOSED-FORM FORMULATION

The trajectory is given by

$$a_t = a^* + (a_0 - a^*)e^{-\omega_{\tau}t}, \quad (45)$$

which depends on (ϕ, ω_{τ}) both through the equilibrium a^* and the exponential term.

Derivative with respect to ϕ : We obtain

$$\frac{\partial a_t}{\partial \phi} = \frac{1 - e^{-\omega_{\tau}t}}{\omega_{\tau}} \quad (46)$$

Interpretation: For large ω_{τ} , the gradient with respect to ϕ saturates quickly but shrinks to scale $\mathcal{O}(1/\omega_{\tau})$, potentially slowing learning of ϕ . Conversely, very small ω_{τ} leads to large steady-state gradients, which may destabilize optimization.

Derivative with respect to ω_{τ} : Here, both the equilibrium and the decay rate depend on ω_{τ} , yielding

$$\frac{\partial a_t}{\partial \omega_{\tau}} = -\frac{\phi}{\omega_{\tau}^2} (1 - e^{-\omega_{\tau}t}) - (a_0 - a^*) t e^{-\omega_{\tau}t}. \quad (47)$$

Interpretation: The gradient with respect to ω_{τ} contains a transient term proportional to $te^{-\omega_{\tau}t}$, which dominates at intermediate times, and a steady-state contribution proportional to $-\phi/\omega_{\tau}^2$, which persists asymptotically. Thus, sensitivity to ω_{τ} is time-dependent, peaking before vanishing exponentially in the transient component.

C.2. Gradient-Based Training

Like Neural ODEs (Chen et al., 2018) and CT-RNNs (Rubanova et al., 2019), NAC produces differentiable computational graphs and can be trained using gradient-based optimization, such as the adjoint sensitivity method (Cao et al., 2003) or backpropagation through time (BPTT) (Le-Cun et al., 1988). In this work, we use BPTT exclusively, as the adjoint sensitivity method can introduce numerical errors (Zhuang et al., 2020).

C.3. Efficiency and Complexity

Table 3 summarizes the computational complexity of different sequence models. For sequence prediction over length n with hidden dimension k , RNNs scale linearly, $\mathcal{O}(nk)$, while Attention and NAC scale quadratically, $\mathcal{O}(n^2k)$. ODE-based models, such as LNNs, incur an additional multiplicative factor S for the number of solver steps. For single-time-step prediction, RNNs and LSTMs require $\mathcal{O}(k)$, whereas Attention and NAC require $\mathcal{O}(nk)$ when recomputing attention over the full sequence.

Table 3. Sequence and time-step prediction complexity. n is the sequence length and k is the hidden/model dimension.

Model	Sequence	Time-step
RNN	$\mathcal{O}(nk)$	$\mathcal{O}(k)$
Attention	$\mathcal{O}(n^2k)$	$\mathcal{O}(nk)$
LNN (ODEsolve)	$\mathcal{O}(nk \cdot S)$	$\mathcal{O}(k \cdot S)$
NAC-Exact	$\mathcal{O}(n^2k)$	$\mathcal{O}(nk)$
NAC-Euler	$\mathcal{O}(n^2k)$	$\mathcal{O}(nk)$

D. Evaluation

D.1. Related Works

The brief description for related works is divided into four subcategories.

DT-RNNs: RNN (Rumelhart et al., 1985) captures sequential dependencies in time-series data by updating a hidden state from the current observation and the previous state. LSTM (Hochreiter & Schmidhuber, 1997) extends RNNs with input, output, and forget gates, allowing the network to maintain and update long-term memory, which improves modeling of long-term dependencies in time-series sequences. GRU (Cho et al., 2014) simplifies the LSTM architecture by combining the forget and input gates into a single update gate, allowing efficient modeling of long-term dependencies in time-series sequences.

CT-RNNs: CT-RNN (Rubanova et al., 2019) model temporal dynamics using differential equations, enabling hidden states to evolve continuously over time in response to inputs, which is particularly useful for irregularly sampled time-series data. PhasedLSTM (Neil et al., 2016) introduces a time gate that updates hidden states according to a rhythmic schedule, enabling efficient modeling of asynchronous or irregularly sampled time-series. GRU-ODE (De Brouwer et al., 2019) extends the GRU to continuous time, evolving hidden states via ODEs to handle sequences with non-uniform time intervals. mmRNN (Lechner & Hasani, 2022) combines short-term and long-term memory units to capture both fast-changing and slowly evolving patterns in sequential data. LTC (Hasani et al., 2021) use neurons with learnable, input-dependent time constants to adapt the speed of dynamics and capture complex temporal patterns in continuous-time data. CfC (Hasani et al., 2022) approximate LTC dynamics analytically, providing efficient continuous-time modeling without relying on numerical ODE solvers.

DT-Attentions: Attention (Vaswani et al., 2017) computes attention weights by measuring similarity between queries and keys, scaling the results, and applying softmax to weigh time-step contributions. Multi-Head Attention (Vaswani et al., 2017) applies multiple parallel scaled dot-product attention mechanisms, capturing different types of temporal dependencies simultaneously for complex time-series modeling.

CT-Attentions: mTAN (Shukla & Marlin, 2021) learns continuous-time embeddings and uses time-based attention to interpolate irregular observations into a fixed-length representation for downstream encoder-decoder modeling. CTA (Chien & Chen, 2021) generalizes discrete-time attention to continuous-time by representing hidden states, context vectors, and attention scores as functions whose dynamics are modeled via neural networks and integrated using ODE solvers for irregular sequences. ODEFormer(d’Ascoli et al., 2023) trains a sequence-to-sequence transformer on synthetic trajectories to directly output a symbolic ODE system from noisy, irregular time-series data. ContiFormer (Chen et al., 2023) builds a continuous-time Transformer by pairing ODE-defined latent trajectories with a time-aware attention mechanism to model dynamic relationships in irregular time-series data.

D.2. Ablations Details

The brief descriptions of variants and ablation are also divided into four subcategories:

Top-K Ablations: *NAC-2k* uses Top- $K=2$ to compute the logits and *NAC-32k* uses Top- $K=32$. All variants use the exact computation mode with 50% sparsity.

Sparsity Ablations: *NAC-02s* uses 20% sparsity to compute the logits and *NAC-09s* uses 90%. *NAC-PW* employs full pairwise (non-sparse) concatenation for input curation. *NAC-FC* replaces the sparse NCP gating mechanism with a simple fully connected layer. All variants use the exact computation mode with Top- $K=8$.

Modes variants: *NAC-Euler* computes attention logits using the explicit Euler integration method. *NAC-Steady* derives attention logits from the steady-state solution of the exact formulation. *NAC-Exact/05s/8k* computes attention logits using the closed-form exact solution. It also overlaps with other ablations, so we combined it into a single one. All modes use Top- $K=8$, 50% sparsity and $\delta_t=1.0$. The sensitivity of NAC to δ_t is visualized in Figure 4

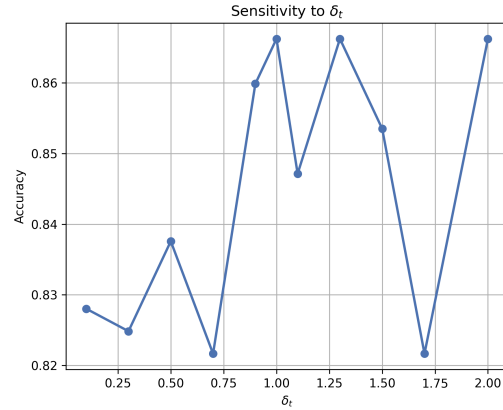


Figure 4. Effect of δ_t on output of NAC.

D.3. Experimental Details

D.3.1. EVENT-BASED MNIST

Dataset Explanation and Curation: The MNIST dataset, introduced by (Deng, 2012), is a widely used benchmark for computer vision and image classification tasks. It consists of 70,000 grayscale images of handwritten digits (0–9), each of size 28×28 pixels, split into 60,000 training and 10,000 testing samples.

Preprocessing: We follow the preprocessing pipeline described in (Lechner & Hasani, 2022), which proceeds as follows. First, a threshold is applied to convert the 8-bit pixel values into binary values, with 128 as the threshold on a scale from 0 (minimum intensity) to 255 (maximum intensity). Second, each 28×28 image is reshaped into a one-dimensional time series of length 784. Third, the binary time series is encoded in an event-based format, eliminating consecutive occurrences of the same value; for example, the sequence $[1, 1, 1, 1]$ is transformed into $(1, t = 4)$. This encoding introduces a temporal dimension and compresses the sequences from 784 to an average of 53 time steps. Finally, to facilitate efficient batching and training, each sequence is padded to a fixed length of 256, and the time dimension is normalized such that each symbol corresponds to one unit of time. The resulting dataset defines a per-sequence classification problem on irregularly sampled time series.

Neural Network Architecture: We develop an end-to-end hybrid neural network by combining compact convolutional layers with NAC or counterparts baselines for fair comparison. Detailed hyperparameters and architectural specifications are provided in Table 4.

D.3.2. PERSON ACTIVITY RECOGNITION (PAR)

Dataset Explanation and Curation: We used the Localized Person Activity Recognition dataset provided by UC Irvine (Vidulin et al., 2010). The dataset comprises 25 recordings of human participants performing different physical activities. The eleven possible activities are “walking,” “falling,” “lying down,” “lying,” “sitting down,” “sitting,” “standing up from lying,” “on all fours,” “sitting on the ground,” “standing up from sitting,” and “standing up from sitting on the ground.” The objective of this experiment is to recognize the participant’s activity from inertial sensors, formulating the task as a per-time-step classification problem. The input data consist of sensor readings from four inertial measurement units placed on participants’ arms and feet. While the sensors are sampled at a fixed interval of 211 ms, recordings exhibit different phase shifts and are thus treated as irregularly sampled time series.

Preprocessing: We first separated each participant’s recordings based on sequence identity and calculated elapsed time in seconds using the sampling period. To

mitigate class imbalance, we removed excess samples from overrepresented classes to match the size of the smallest class. Subsequently, the data were normalized using a standard scaler. Finally, the dataset was split into a 90:10 ratio for training and testing.

Neural Network Architecture: Following the approach in Section D.3.1, we developed an end-to-end hybrid neural network combining convolutional heads with NAC or other baselines. Hyperparameter details are summarized in Table 4.

D.3.3. AUTONOMOUS VEHICLE

Dataset Explanation and Curation: We followed the data collection methodology described in (Razzaq & Hongwei, 2023). For OpenAI-CarRacing, a PPO-trained agent (5M timesteps) was used to record 20 episodes, yielding approximately 48,174 RGB images of size $92 \times 92 \times 3$ with corresponding action labels across five discrete actions (no-act, move left, forward, move right, stop). The dataset was split with 10% reserved for testing and the remaining 90% for training. For the Udacity simulator, we manually controlled the vehicle for 50 minutes, producing 15647 RGB images of size $320 \times 160 \times 3$, captured from three camera streams (left, center, right) along with their corresponding continuous steering values. This dataset was split into 20% testing and 80% training.

Preprocessing: No preprocessing was applied to the OpenAI-CarRacing dataset. For the Udacity simulator, we followed the preprocessing steps in (Shibuya, 2017). Each image was first cropped to remove irrelevant regions and resized to $66 \times 120 \times 3$. Images were then converted from RGB to YUV color space to match the network input. To improve robustness, data augmentation techniques, including random flips, translations, shadow overlays, and brightness variations, were applied to simulate lateral shifts and diverse lighting conditions.

Neural Network Architecture: For OpenAI-CarRacing, we modified the neural network architecture proposed in (Razzaq & Hongwei, 2023), which combines compact CNN layers for spatial feature extraction with LNNs to capture temporal dynamics. In our implementation, the LNN layers were replaced with NAC and its comparable alternatives for fair evaluation. Full hyperparameter configurations are provided in Table 4. For the Udacity simulator, we modified the network proposed in (Bojarski et al., 2016) by replacing three latent MLP layers with NAC and its counterparts. Full hyperparameters for this configuration are summarized in Table 4.

Saliency Maps: A saliency map visualizes the regions of the input that a model attends to when making decisions. Figure 5 shows the saliency maps for the OpenAI CarRacing environment. We observe that only NAC (Steady, Euler,

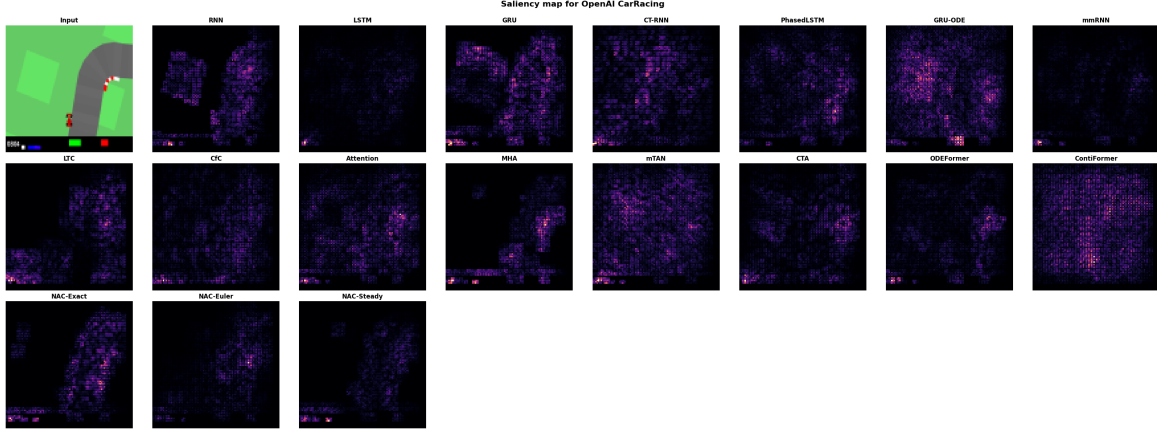


Figure 5. Saliency maps for OpenAI CarRacing

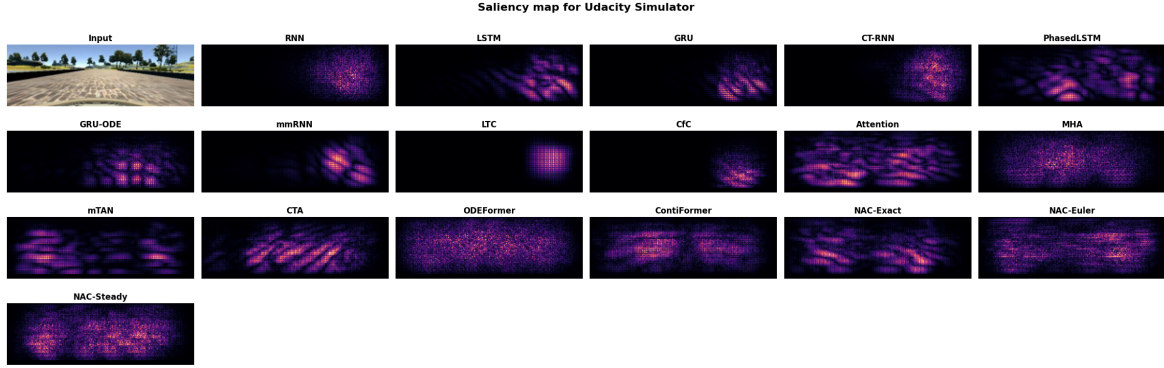


Figure 6. Saliency maps for Udacity Simulator

and Steady) maintains focus on the road’s horizon, while other models either focus on the sides or remain largely unresponsive to the task. Figure 6 also presents the saliency maps for the Udacity Simulator. In this case, NAC-Exact, CTA produces the most accurate visual maps, maintaining attention on the road’s horizon, followed by ContiFormer and mTAN, which achieve comparable performance. Attention and PhasedLSTM also generate reasonable saliency maps, although their focus is more dispersed across the scene. In contrast, other models either fail to identify relevant regions, producing blurry maps, or focus solely on one side of the road. These results demonstrate the NAC’s ability to understand the underlying task.

D.3.4. INDUSTRY 4.0

Dataset Explanation and Curation: *PRONOSTIA* dataset is a widely recognized benchmark dataset in the field of condition monitoring and degradation estimation of rolling-element bearings. Nectoux et al.(Nectoux et al., 2012) developed this dataset as part of the PRONOSTIA experimental platform. The dataset comprises 16 complete run-to-failure experiments performed under accelerated wear conditions

Algorithm 3 Time–frequency Representation Algorithm

Require: windowed signal I_w , critical frequency f_c , operating frequency f_o , sampling period $T_{sampling}$, windowed physical constraints (t_w, T_w)
 $a_{min} = \frac{f_c}{f_{max} \cdot T_{sampling}}$, $a_{max} = \frac{f_c}{f_{min} \cdot T_{sampling}}$,
 $a_{scale} \in [a_{min}, a_{max}]$
 $I_{TFR} \leftarrow \{\}$
for (i_w, t_w, T_w) in (I_w, t_w, T_w) : **do**
 Wavelets: $\Gamma_{iw}(a, b) = \int_{-\infty}^{\infty} i_w \psi^* \left(\frac{t-b}{a} \right) dt$.
 Energy: $E = \sum_{m=1}^M |\Gamma_{iw}(a, b)|^2$
 Dominant frequency: $f_d = a_{scale} [\arg \max(E)]$.
 Entropy: $h = - \sum_{i=m}^M P(i_w(t)) \log P(i_w(t))$.
 Kurtosis: $K = \frac{\mathbb{E}[(i_w(t) - \mu)^4]}{\sigma^4}$.
 Skewness: $sk = \frac{\mathbb{E}[(i_w(t) - \mu)^3]}{\sigma^3}$.
 mean: $\mu = \frac{1}{M} \sum_{m=1}^M i_w(m)$.
 standard deviation: $\sigma = \sqrt{\frac{1}{M} \sum_{i=1}^M (i_w(m) - \mu)^2}$.
 $X_n \leftarrow [\log(E), f_d, h, K, sk, \mu, \sigma]$
end for
return $I_{TFR} = \text{Concat}(X_1, X_2 \dots X_{N_s}, t_n, T_n)$

Table 4. Summary of Key Hyperparameters of All Experiments

Param.	MNIST	PAR	CarRacing	Udacity	RUL EST.
Conv layers	2×1D(64@5)	1D(64@5, 64@3)	3×TD-2D(10–30@3–5)	5×2D(24–64@5–3, ELU)	2×1D(32@3, 16@2)
NAC	64-d, 8h	32-d, 4h	64-d, 16h	100-d, 16h	16-d, 8h
Dense	32–10(SM)	32–11(SM)	64–5(SM)	64–1(Lin)	1(Lin)
Dropout	–	–	0.2	0.5	–
Opt.	AdamW	AdamW	Adam	AdamW	AdamW
LR	0.001	0.001	0.0001	0.001	0.001
Loss	SCE	SCE	SCE	MSE	MSE
Metric	Acc	Acc	Acc	MAE	Score
Batch	32	20	32	–	32
Epochs	150	500	100	10	150

Note: SCE = Sparse Categorical Crossentropy; Acc = Accuracy; MAE = Mean Absolute Error; MSE = Mean Squared Error; SM = softmax; Lin = Linear; TD = TimeDistributed; Conv1D/2D = Conv1D/2D; d = model dimension; h = attention heads.

Baselines Hyperparameters Clarification: All (CT & DT) RNNs use the same number of hidden units as NAC’s d_{model} , and all (DT & CT) Attention use the same d_{model} and *heads* as NAC. The other layers, including 1D/2D, Dense, and the remaining hyperparameters, are the same during our tests.

Table 5. Data distributions of PRONOSTIA, XJTU-SY, and HUST datasets.

Dataset	Condition	Frequency	Radial Load	Speed	Train	Test
PRONOSTIA	Condition 1	100 Hz	4 kN	1800 rpm	4 ~ 7	1 ~ 3
	Condition 2	100 Hz	4.2 kN	1650 rpm	–	1 ~ 7
	Condition 3	100 Hz	5 kN	1500 rpm	–	1 ~ 3
XJTU-SY	Condition 1	35 Hz	4 kN	2100 rpm	–	1 ~ 5
	Condition 2	37.5 Hz	4.2 kN	2250 rpm	–	1 ~ 5
	Condition 3	40 Hz	5 kN	2400 rpm	–	1 ~ 5
HUST	Condition 1	–	0 W	–	–	1 ~ 5
	Condition 2	–	200 W	–	–	1 ~ 5
	Condition 3	–	400 W	–	–	1 ~ 5

Note: The PRONOSTIA dataset is utilized for training and generalization testing, while the XJTU-SY and HUST datasets are employed to evaluate cross-validation testing. (–) values are either not available or not utilized.

across three different operating settings: 1800 rpm with 4 kN radial load, 1650 rpm with a 4.2 kN load, and 1500 rpm with a 5 kN load, all at a frequency of 100 Hz. Vibration data were recorded using accelerometers placed along the horizontal and vertical axes, which were sampled at 25.6 kHz. Additionally, temperature readings were collected at a sampling rate of 10 Hz. The data distributions for training and testing are provided in Table 5.

XJTU-SY Dataset is another widely recognized benchmark dataset developed through collaboration between Xi’an Jiaotong University and Changxing Sumyoung Technology (Wang et al., 2018). The dataset comprises 15 complete run-to-failure experiments performed under accelerated degradation conditions with three distinct operational settings: 1200 rpm (35 Hz) with a 12 kN radial load, 2250 rpm (37.5 Hz) with an 11 kN radial load, and 2400 rpm (40 Hz) with a 10 kN radial load. Vibrational signals were recorded using an accelerometer mounted on the horizontal and vertical axes and sampled at 25.6 kHz. This dataset is only used for the

cross-validation test.

HUST Dataset is a practical dataset developed by Hanoi University of Science and Technology to support research on ball bearing fault diagnosis (Hong & Thuan, 2023). The dataset includes vibration data collected from five bearing types (6204, 6205, 6206, 6207, and 6208) under three different load conditions: 0 W, 200 W, and 400 W. Six fault categories were introduced, consisting of single faults (inner race, outer race, and ball) and compound faults (inner–outer, inner–ball, and outer–ball). Faults were created as early-stage defects in the form of 0.2 mm micro-cracks, simulating real degradation scenarios. The vibration signals were sampled at 51.2 kHz with approximately 10-second recordings for each case. This dataset is only used for the cross-validation test.

Preprocess: Condition monitoring data comprises 1D non-stationary vibrational signals collected from multiple sensors. To extract meaningful information, these signals must be transformed into features that possess meaningful physi-

cal interpretability. We utilized the preprocessing proposed in (Razzaq & Zhao, 2025a) and labels are generated according to (Razzaq & Zhao, 2025b). Initially, the signal is segmented into small, rectangularized vectors using a windowing technique (w), enabling better localization of transient characteristics. The continuous wavelet transform (CWT) (Aguiar-Conraria & Soares, 2014) with the Morlet wavelet (Lin & Qu, 2000) as the mother wavelet is then applied to obtain a time-frequency representation (TFR). The CWT is defined as $\Gamma(a, b) = \int_{-\infty}^{\infty} x_w(t) \frac{1}{\sqrt{a}} \psi^* \left(\frac{t-b}{a} \right) dt$, where a and b denote the scale and translation parameters, respectively, and ψ is the Morlet wavelet function. From the resulting TFR, a compact set of statistical and domain-specific features is extracted to characterize the operational condition of the bearing. The complete feature extraction procedure is described in Algorithm 3.

Neural Network Architecture: The objective of this problem is to design a compact neural network that can effectively model degradation dynamics while remaining feasible for deployment on resource-constrained devices, enabling localized and personalized prognostics for individual machines. To achieve this, we combine a compact convolutional network with NAC. The CNN component extracts spatial degradation features from the training data, while NAC performs temporal filtering to emphasize informative features. This architecture maintains a small model size without sacrificing representational capacity. Full hyperparameter configurations are reported in Table 4.

Evaluation Metric: Score is a metric specifically designed for RUL estimation in the IEEE PHM (Nectoux et al., 2012) to score the estimates. The scoring function is asymmetric and penalizes overestimations more heavily than early predictions. This reflects practical considerations, as late maintenance prediction can lead to unexpected failures with more severe consequences than early intervention can.

$$Score = \sum_{i: \hat{y}_i < y_i} \left(e^{-\frac{\hat{y}_i - y_i}{13}} - 1 \right) + \sum_{i: \hat{y}_i \geq y_i} \left(e^{\frac{\hat{y}_i - y_i}{10}} - 1 \right) \quad (48)$$